Capillarity

Vol. 4, No. 2, p. 31-44, 2021

Original article

Investigation of the dynamics of immiscible displacement of a ganglion in capillaries

Amgad Salama[1]*, Jianchao Cai[2], Jisheng Kou[3], Shuyu Sun[4], Mohamed F. El-Amin[5], Yi Wang[6]

[1]*Process System Engineering, Faculty of Engineering and Applied Science, University of Regina, SK S4S 0A2, Canada*

[2]*State Key Laboratory of Petroleum Resources and Prospecting, China University of Petroleum, Beijing 102249, P. R. China*

[3]*School of Civil Engineering, Shaoxing University, Shaoxing 312000, P. R. China*

[4]*Computational Transport Phenomena Laboratory, Physical Science and Engineering Division, King Abdullah University of Science and Technology, Thuwal 23955-6900, Saudi Arabia*

[5]*College of Engineering, Effat University, Jeddah 21478, Saudi Arabia*

[6]*National Engineering Laboratory for Pipeline Safety, China University of Petroleum, Beijing 102249, P. R. China*

Keywords:
Imbibition
drainage
ganglion
capillarity

Cited as:
Salama, A., Cai, J., Kou, J., Sun, S., EI-Amin, M. F., Wang, Y. Investigation of the dynamics of immiscible displacement of a ganglion in capillaries. Capillarity, 2021, 4(2): 31-44, doi: 10.46690/capi.2021.02.02

Abstract:
In this work the problem of displacing a ganglion of a fluid by another immiscible one in capillaries is investigated. A modeling approach is developed to predict the location of the ganglion with time. The model describes two patterns; namely, when the ganglion totally exists inside the tube, and when the advancing interface of the ganglion has broken through the exit of the tube. The model is valid for the case in which the ganglion is wetting as well as when it is nonwetting to the wall of the tube. It also considers the situation in which both the advancing and the receding interfaces assume, generally, different contact angles. For the special case when the displacement process is quasistatic, both the receding and the advancing contact angles may be considered the same. Under these conditions, interfacial tension force plays no role and the ganglion moves as a plug inside the tube with a constant velocity. When the viscosity ratio between the invading fluid and the ganglion is one (i.e., both phases are having the same viscosity) the motion reduces to the Hagen-Poiseuille flow in pipes. Once the advancing interface breaks through the exit of the tube, interfacial tension starts to take part in the displacement process and the ganglion starts to accelerate or decelerate according to the viscosity ratio. When the ganglion is nonwetting, interfacial tension becomes in the direction of the flow and is opposite to the flow otherwise. The model accounts for external forces such as pressure and gravity in addition to capillarity. A computational fluid dynamics analysis of this system is conducted for both types of wettability scenarios and shows very good match with the results of the developed model during both the two modes of flow patterns. This builds confidence in the developed modeling approach. Other cases have also been explored to highlight the effects of other scenarios.

1. Introduction

In oil production, water is injected into oil reservoirs, in a process called water flooding, to displace the oil towards production wells (Abdus et al., 2008; Ahmed, 2019; Arab et al., 2020; Mogensen and Masalmeh, 2020). Even though this technique is widely used worldwide, it can only displace but portion of the in-place oil. Indeed, it has been reported that the average residual oil left in the reservoir is perhaps one-third of the original oil (Jha, 1984; Sheng, 2013; Salama et al., 2017; Speight, 2019). Such substantial quantities of residual oil are consequence of water bypassing chunks of oil intact in the rock pores. Many factors may contribute to such phenomenon including heterogeneity of reservoir materials and of their affinities towards reservoir fluids. In fact, it has

Yandy Scientific Press

*Corresponding author.
E-mail address: amgad.salama@uregina.ca (A. Salama); caijc2016@hotmail.com (J. Cai); jishengkou@163.com (J. Kou); shuyu.sun@kaust.edu.sa (S. Sun); mohamed.elamin.kaust@gmail.com (M. F. EI-Amin); wangyi1031@cup.edu.cn (Y. Wang).
2709-2119 © The Author(s) 2021.
Received May 10, 2021; revised May 30, 2021; accepted June 1, 2021; available online June 3, 2021.

been reported (Zhong et al., 2014; Bao et al., 2018) how the differences in affinity properties of a Y-shaped pore junction can influence the amount of oil advancing in the two branches. The displacement of oil by water depends on many factors including oil viscosity and rock characteristics. The process of water flooding measures how water displaces oil from porous and permeable reservoir rocks at a microscopic scale, which represents the level of analysis over a small core-plug sample in a laboratory. At the reservoir scale, however, the efficiency of waterflooding processes must include information about the effects of geology, gravity, and geometry. Because of the small length scale associated with the displacement process at the scale of individual pores, capillary force plays crucial role in the sweeping efficiency. The study of this mechanism at pore scale can be conducted in two ways; namely, via pore network models (Raoof and Hassanizadeh, 2010; Raoof et al., 2013; Xiong et al., 2016; Huang et al., 2020; Won et al., 2021), or via a real reconstruction of a representative porous medium domain via techniques involving computer tomography (CT scan) (Alemu et al., 2011; Cnudde et al., 2011; Madonna et al., 2012; Ramanathan et al., 2016; Bageri et al., 2021). Of the two, pore network models represent the simplest to establish. In pore network models two techniques have been adapted; the first is quasistatic pore network models (Blunt et al., 2002; Nordhaug et al., 2003; Zhang et al., 2015; Regaieg and Moncorgé, 2017) and the second is dynamic pore network models (Blunt, 2001; Joekar-Niasar and Hassanizadeh, 2011; Joekar-Niasar and Hassanizadeh, 2012; Qin and van Brummelen, 2019). In quasistatic pore network models, certain rules are set to advance the interfaces through pore bodies and pore throats. A critical entry pressure is defined for every pore throat in the network. These entry pressure values define criteria for the interface to advance into pore throat or otherwise pining at its entry. The critical entry pressure is calculated based on the static contact angle, interfacial tension, and the diameter of the pore. An algorithm may be developed to monitor how the network is populated with the invading fluid until breakthrough occurs. Occasionally, invaded fluid may get separated and trapped in certain locations of the network and defines what is called ganglions. In dynamic pore network models, on the other hand, the velocity of the interface is correlated with the pressure difference via a conductance term that accounts for the resistances to the flow in each pore throat. Two general approaches, exist; namely single-pressure and two-pressure algorithms (Joekar-Niasar and Hassanizadeh, 2012). In single-pressure algorithm, a single pressure is assigned to each pore body regardless of their fluid occupancy. In two-pressure algorithm, when a pore body is filled with two fluids, each fluid is assumed to have its own pressure and, in this case, a local capillary pressure exists in a pore body. When the invaded phase exists as separated ganglions, things become more complex by the possible larger number of interfaces a ganglion could establish within the network branches. In microscale simulation, on the other hand, real pore structures within a representative sample are extracted and conservation laws are solved in the pore space where the two fluids coexist (Almetwally and Jabbari, 2020). While this approach is more realistic, it cannot be used on relatively larger-scale volumes for the relatively larger computational resources it requires. Different numerical techniques have been adapted to study the displacement of one fluid by another immiscible one. They may, generally, categorized into three basic models. These are, namely; sharp interface models (Sato and Ničeno, 2013; Bao et al., 2016; Montazeri et al., 2017; Xu et al., 2018), diffuse interface models (De Mello and da Silveira Filho, 2005; Pan 2019; Benilova, 2020), and lattice Boltzmann models (Grunau et al., 1993; Lamura et al., 1999; Guo, 2021). The outcomes of these methods on a small-scale representative sample may be extrapolated and upscaled to provide field variables.

Another application where displacement of immiscible fluids in capillaries occur is related to the filtration of oily water systems using membrane technology. In this case, oil exists as droplets dispersed in the continuous water phase. In order for the membrane to function effectively in separating oil and water, the selectivity of the membrane is not only dependent on its pore sizes but also on the affinity characteristics towards both oil and water. In other words, the membrane should be selected to be oleophobic such that interfacial forces act to hold oil droplets at the surface of the membrane. If the transmembrane pressure is held smaller than the entry pressure, oil droplets will remain pinned at the pore openings without permeation. The accumulation of oil droplets at the surface of the membrane intensifies the problem of fouling and reduces the filtration capacity of the membrane. In order to minimize the potential growth of fouling, pinned droplets must dislodge the surface. This is done via enforcing the feed emulsion along the membrane surface in crossflow methodology. The shear flow stresses pinned droplets to detach the surface and free pore openings from blockage (Tummons et al., 2016; Zoubeik et al., 2018; Salama, 2020a, 2020b, 2020c, 2020d, 2021b, 2021c; Echakouri et al., 2021). In some scenarios, the crossflow field can breakup permeating droplets into two parts one remains at the surface and another inside the pore (i.e., a ganglion). The ganglion further permeates via the pore by permeate flux. It is interesting to estimate the volume of the droplet that remains in the pore and to highlight the displacement of the droplet by permeate flux. This has been the topic of previous works by Salama (2020c) in which a computational fluid dynamics (CFD) analysis has been used to highlight the physics involved in such process.

From the previous discussion, it can be seen that handling the problem of displacement of a fluid by another immiscible can be quite involved particularly in complex geometries. For the scale of such phenomenon in capillary tubes, Salama (2021a) has recently developed a generalized model that accounts for all possible scenarios involving imbibition and drainage processes. Another case that can be of interest in this category would be related to the scenario in which a fluid is displacing a ganglion of another immiscible one in capillaries. This is the topic of this work where we try to extend the framework developed by Salama (2021a) to encounter the movement of ganglions in capillaries.

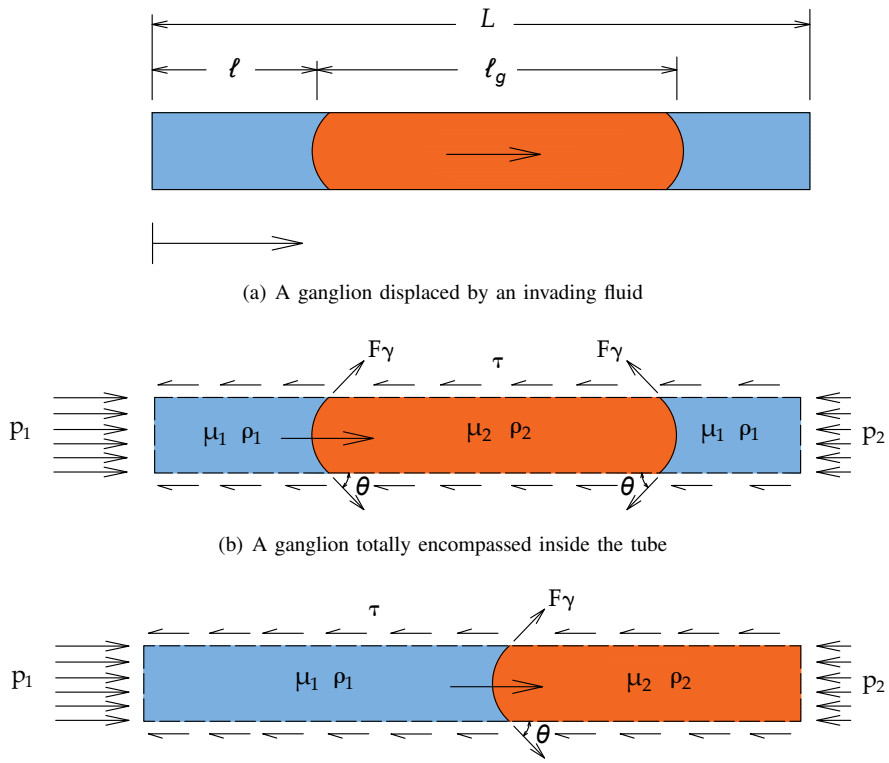

(a) A ganglion displaced by an invading fluid

(b) A ganglion totally encompassed inside the tube

(c) A ganglion starting to break through the exit of the tube

Fig. 1. Schematic of the considered setup where a ganglion is enclosed inside a capillary tube and is surrounded by the other immiscible fluid (a). Two patterns are identified; namely, when the ganglion is totally contained inside the tube (b), and when the ganglion has broken through the exit (c).

2. Problem statement

As indicated earlier, water bypassing oil during water flooding can lead to larger volume of oil left intact inside the reservoir. Furthermore, due to the higher viscosity contrast between water and the oil, with the less viscous water displacing the higher viscosity oil, fingering can occur at the water-oil front that can lead to the separation of chunks of oil from the bulk oil where they become surrounded by water. In other words, ganglions are formed in the interface region that are transported with the invading water phase. It is therefore important to investigate their dynamics in simplified geometries before featuring their behavior in complex systems. The considered setup represents a capillary tube where a ganglion initially exists in the tube and is displaced by an invading immiscible fluid. Fig. 1(a) shows a schematic of the considered setup where a ganglion (orange in color) is displaced by an immiscible one (blue in color). The length of the ganglion is l_g and the location of its receding interface from the start of the tube is l with the total length of the tube given as L. Two flow patterns can establish; namely, 1) when the ganglion is fully encompassed inside the tube, Fig. 1(b), and 2) when the advancing interface has breakthrough the exit of the tube, Fig. 1(c). Both flow patterns are treated separately and a model that depicts the location of the ganglion in both cases would need to be developed. The basic assumptions related to the developed model is that both fluids are incompressible and in the special case of slower flow, both the interfaces of the ganglion assume, approximately, the same contact angle.

3. Model development

The governing equation that describes the dynamics of the ganglion inside a capillary tube during an invasion process by another immiscible fluid is the conservation of momentum, which may be written over a control volume as:

$$\frac{\partial}{\partial t}\int_V \rho \mathbf{u} dV + \int_A (\rho \mathbf{u}\cdot\mathbf{n})\mathbf{u} dA = \sum \mathbf{F} \tag{1}$$

where $\mathbf{u}$ is the velocity vector, $\mathbf{n}$ is the outwardly unit normal vector to the surface area A, and $\mathbf{F}$ refers to all external volume and surface forces. In typical flows in capillaries, the inertia term may be neglected (Lucas, 1918; Washburn, 1921; Dullien et al., 1977; Hammecker et al., 1993; Cai et al., 2010, 2012, 2021; Bijeljic et al., 2011; Salama, 2021a) and the above equation reduces to:

$$\sum \mathbf{F} = 0 \tag{2}$$

The set of external forces include, pressure, capillary, gravity and friction forces and they may be calculated as:

$$\sum \mathbf{F} = -\int_A p\mathbf{n} dA + \int_A \tau \mathbf{n} dA + \int_V \rho \mathbf{g} dV + \int_{CL} \gamma \mathbf{t} dl \tag{3}$$

where γ is the interfacial tension, $\mathbf{t}$ is the unit vector in the plane tangent to the interface at the contact line (CL) and normal to the CL. Let us define the average shear stress $\bar{\tau}$ as:

$$\overline{\tau} = \frac{1}{A_\tau} \int_{A_\tau} \tau dA \tag{4}$$

where A_τ refers to the area where the shear stress applies. Eq. (3) would now be adapted over the control volume that represents the capillary tube. We apply this equation for the two patterns discussed before.

3.1 Case I: the ganglion is totally enclosed in the tube

When the ganglion is totally contained within the capillary tube, one can establish two scenarios. The first represents the case in which the ganglion is wetting and the second is when the ganglion is nonwetting. Fig. 2 shows schematic of the two cases in which the flow is directed downwards. The ganglion establishes two interfaces inside the capillary tube. Under static conditions, these interfaces assume the static contact angle. The advancement of the ganglion inside the capillary tube, however, results in the two interfaces (i.e., the advancing and the receding interfaces) to assume different contact angles; namely the advancing and the receding contact angles. Such dynamic contact angles are, generally, function of the flow velocity (Payatakes, 1982; Wu et al., 2017; Siebold et al., 2020). In this case, one can break the forces influencing the dynamics of the ganglion inside the tube for the two cases as:

$$\begin{aligned}\sum F = &(p_1 - p_2) A_{CS} - \pi D (L - l_g) \overline{\tau}_1 - \pi D l_g \overline{\tau}_2 \\ &\pm \rho_1 g (L - l_g) A \pm \rho_2 g l_g A \pm \pi D \gamma (\cos\theta_A - \cos\theta_R)\end{aligned} \tag{5}$$

where the plus sign in the interfacial tension term represents the case of a wetting ganglion and the negative sign for a nonwetting ganglion. In the above equation, A_{CS} is the cross-sectional area of the tube. Likewise, the $\pm$ sign in the gravity term indicates that the gravity could be in the direction of the flow or opposite to it.

In typical flows in capillary tubes, it is customary to assume that the flow is laminar and the velocity profile is parabolic (i.e., lower Reynolds number flow conditions). In this case, the average shear stress in the two fluid regions may be expressed as (Salama, 2021a):

$$\overline{\tau}_1 = 8\mu_1 \frac{U}{D}, \quad \overline{\tau}_2 = 8\mu_2 \frac{U}{D} \tag{6}$$

where U is the average velocity. Ignoring inertia and substitution into Eq. (5), one obtains:

$$\begin{aligned}\Delta p A_{CS} - 8\mu_1 \pi (L - l_g) U - 8\mu_2 \pi l_g U \pm \rho_1 g (L - l_g) A \\ \pm \rho_2 g l_g A \pm \pi D \gamma (\cos\theta_A - \cos\theta_R) = 0\end{aligned} \tag{7}$$

With some manipulations and rearrangements, Eq. (7) reduces to:

$$\begin{aligned}\Delta p A_{CS} - 8\mu_2 \pi U L \left[\frac{\mu_1}{\mu_2}\left(1 - \frac{l_g}{L}\right) + \frac{l_g}{L}\right] \\ \pm \rho_2 g A_{CS} L \left[\frac{\rho_1}{\rho_2}\left(1 - \frac{l_g}{L}\right) + \frac{l_g}{L}\right] \\ \pm \pi D \gamma (\cos\theta_A - \cos\theta_R) = 0\end{aligned} \tag{8}$$

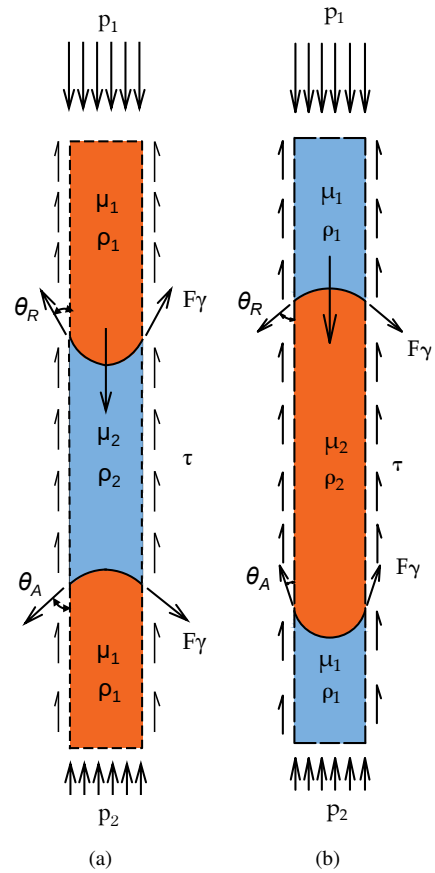

Fig. 2. A wetting (a) and a nonwetting (b) ganglions inside the capillary tube: (a) A wetting ganglion; (b) A nonwetting ganglion.

Following Salama (2021a), let both the viscosity and density ratios be defined as: $\lambda = \mu_1/\mu_2$ and $\xi = \rho_1/\rho_2$, substitution in Eq. (8) yields:

$$\begin{aligned}\Delta p A_{CS} - 8\mu_2 \pi U L \left[\lambda\left(1 - \frac{l_g}{L}\right) + \frac{l_g}{L}\right] \\ \pm \rho_2 g A_{CS} L \left[\xi\left(1 - \frac{l_g}{L}\right) + \frac{l_g}{L}\right] \\ \pm \pi D \gamma (\cos\theta_A - \cos\theta_R) = 0\end{aligned} \tag{9}$$

The average velocity, U, may be defined as: $U = dl/dt$ (Salama, 2021a), which is shown in Fig. 1(a), in this case Eq. (9) reduces to:

$$\begin{aligned}\Delta p A_{CS} - 8\mu_2 \pi L \left[\lambda\left(1 - \frac{l_g}{L}\right) + \frac{l_g}{L}\right] \frac{dl}{dt} \\ \pm \rho_2 g A_{CS} L \left[\xi\left(1 - \frac{l_g}{L}\right) + \frac{l_g}{L}\right] \\ \pm \pi D \gamma (\cos\theta_A - \cos\theta_R) = 0\end{aligned} \tag{10}$$

Dividing thoroughly by A_{CS} and rearrangement, one obtains:

$$\begin{aligned}\frac{32\mu_2 L}{D^2}\left[\lambda\left(1 - \frac{l_g}{L}\right) + \frac{l_g}{L}\right] \frac{dl}{dt} = \\ \Delta p \pm \rho_2 g L \left[\xi\left(1 - \frac{l_g}{L}\right) + \frac{l_g}{L}\right] \pm \Delta p_c\end{aligned} \tag{11}$$

where $\Delta p_c = 4\gamma/D(\cos\theta_A - \cos\theta_R)$. Let us define the parameters a_μ, and a_g as:

$$a_\mu = \frac{32\mu_2 L}{D^2}\left[\lambda\left(1-\frac{l_g}{L}\right)+\frac{l_g}{L}\right] \tag{12}$$

$$a_g = \rho_2 g L\left[\xi\left(1-\frac{l_g}{L}\right)+\frac{l_g}{L}\right] \tag{13}$$

Substitution into Eq. (11), one obtains:

$$\frac{dl}{dt} = \frac{\Delta p \pm \Delta p_c \pm a_g}{a_\mu} \tag{14}$$

Eq. (14) is an implicit equation since $\Delta p_c = f(dl/dt, \gamma, D, \theta_S)$, where θ_S is the static contact angle. In the special case when the flow is relatively slow, both the advancing and the receding interfaces assume approximately the static contact angle. In this case, one may assume $\Delta p_c = 0$ and the above equation reduces to:

$$\frac{dl}{dt} = \frac{\Delta p \pm a_g}{a_\mu} \tag{15}$$

The right-hand side of Eq. (15) is constant, and this implies that the average velocity is constant. For this scenario, let us consider the case when $\lambda = 1$, (i.e., $\mu_1 = \mu_2 = \mu$), for flow in horizontal tube (i.e., $a_g = 0$), the parameter a_μ becomes equal to $32\mu L/D^2$ and Eq. (15) becomes:

$$\frac{dl}{dt} = U = \frac{D^2}{32\mu L}\Delta p \tag{16}$$

Which conforms to the Hagen-Poussile's formula (Batchelor, 2000). Integrating Eq. (15), yields:

$$l(t) = \left(\frac{\Delta p}{a_\mu} \pm \frac{a_g}{a_\mu}\right)t \tag{17}$$

Eq. (17) indicates that the location of the ganglion proceeds linearly with time and the ganglion is not accelerating during this flow pattern.

3.2 Case II: the advancing interface has exited the tube

When the ganglion is fully contained inside the capillary tube, the size of the two fluid regions remains constant. In this case, pressure, gravity, friction, interfacial tension forces are constant. This would not be the case when the ganglion starts to break through the exit, $(l + l_g > L)$. The size of the invading fluid continuously increases while the size of the invaded fluid diminishes. This implies that the friction force changes continuously as the makeup of the fluid in the tube changes. This flow pattern is similar to the cases recently studied in (Salama, 2021a) that describes the displacement of one fluid by another immiscible one in capillaries. For the sake of completion, however, we highlight the main steps. For this case, Eq. (5) is modified to incorporate the effects of capillarity of the single interface that exists inside the tube, therefore one obtains:

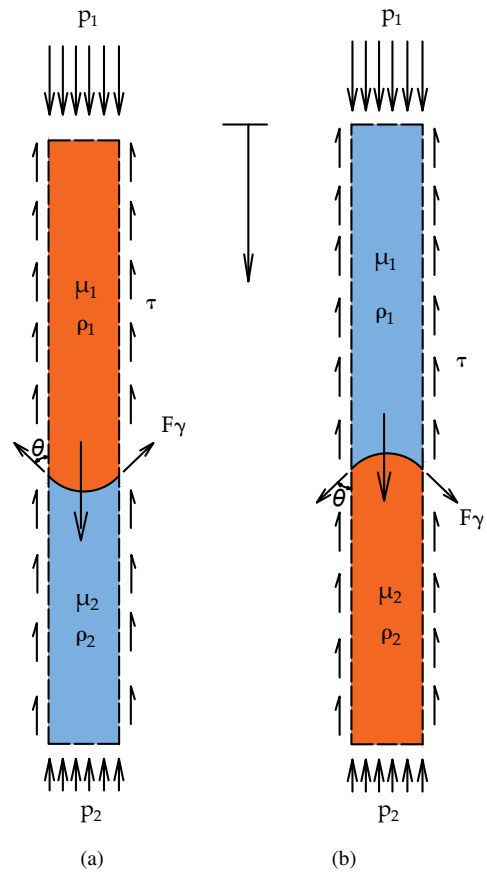

Fig. 3. When the ganglion has broken through the exit of the tube, a single interface remains inside the tube which is displaced towards the exit of the tube. In this case the volume of the invading fluid inside the tube increases and that of the ganglion decreases: (a) Invasion by a nonwetting phase; (b) Invasion by a wetting phase.

$$\sum F = (p_1 - p_2)A_{CS} - \int_{A_1}\tau_1 dA - \int_{A_2}\tau_2 dA \pm \int_{V_1}\rho_1 g dV \pm \int_{V_2}\rho_2 g dV \pm \pi D\gamma\cos\theta \tag{18}$$

where p_1 and p_2 are the pressures at the inlet and exit of the tube, τ_1 and τ_2 are the shear stresses at the wall of the two parts of the control volume, A_1 and A_2 are the surface areas of the control volume associated with the two fluid regions (as shown in Fig. 3), V_1 and V_2 are the volumes of the respective two fluid regions, ρ_1 and ρ_2 are the densities of the fluids in the two parts, A_{CS} is the cross-sectional area, and θ is the contact angle.

Adapting Eq. (18) to the control volume considered in Fig. 3, and ignoring inertia term, one obtains:

$$(p_1 - p_2)A_{CS} - \pi D l\overline{\tau}_1 - \pi D(L-l)\overline{\tau}_2 \pm \rho_1 g l A \pm \rho_2 g(L-l)A \pm \pi D\gamma\cos\theta = 0 \tag{19}$$

Substitution of Eq. (6) into Eq. (19) and dropping the subscript CS, one gets:

$$\Delta p A - 8\pi L\mu_1 U - 8\pi(L-l)\mu_2 U \pm \rho_1 g l A \pm \rho_2 g(L-l)A \pm \pi D\gamma\cos\theta = 0 \tag{20}$$

As has been introduced before, the average velocity U may be correlated with the time derivative of the location of the meniscus as $U = dl/dt$, where t is the elapsed time. Substitution into Eq. (20) yields:

$$\begin{aligned}\Delta pA \pm \rho_1 glA \pm \rho_2 g(L-l)A - 8\pi l\mu_1 \frac{dl}{dt} \\ - 8\pi(L-l)\mu_2 \frac{dl}{dt} \pm \pi D\gamma\cos\theta = 0\end{aligned} \tag{21}$$

Factoring and collection of terms, one obtains:

$$\begin{aligned}\Delta p \pm \frac{4\gamma\cos\theta}{D} \pm \rho_2 gL\left[\frac{l}{L}(\xi-1)+1\right] \\ - \frac{32\mu_2(\lambda-1)}{D^2} l\frac{dl}{dt} - \frac{32\mu_2 L}{D^2}\frac{dl}{dt} = 0\end{aligned} \tag{22}$$

With the capillary pressure defined as $p_c = 4\gamma\cos\theta/D$, substitution in the above equation and dividing thoroughly by $|p_c|$, one obtains:

$$\begin{aligned}\left[\frac{\Delta p}{|p_c|} \pm \frac{p_c}{|p_c|} \pm \frac{\rho_2 gL}{|p_c|} \pm \frac{\rho_2 g}{|p_c|}(\xi-1)l\right] - \\ \left[\frac{32\mu_2}{|p_c|D^2}(\lambda-1)l + \frac{32\mu_2 L}{|p_c|D^2}\right]\frac{dl}{dt} = 0\end{aligned} \tag{23}$$

Rearrangement, one gets:

$$\begin{aligned}\left[\frac{32\mu_2}{|p_c|D^2}(\lambda-1)l + \frac{32\mu_2 L}{|p_c|D^2}\right]\frac{dl}{dt} - \left[\pm\frac{\rho_2 g}{|p_c|}(\xi-1)\right]l \\ = \frac{\Delta p}{|p_c|} \pm \frac{p_c}{|p_c|} \pm \frac{\rho_2 gL}{|p_c|}\end{aligned} \tag{24}$$

Following Salama (2021a), let the parameters, a, b, c, and d be defined as:

$$a = \frac{32\mu_2}{|p_c|D^2}(\lambda-1) \tag{25}$$

$$b = \frac{32\mu_2 L}{|p_c|D^2} \tag{26}$$

$$c = \pm\frac{\rho_2 g}{|p_c|}(\xi-1) \tag{27}$$

$$d = \frac{\Delta p}{|p_c|} \pm \frac{p_c}{|p_c|} \pm \frac{\rho_2 gL}{|p_c|} \tag{28}$$

Eq. (24), therefore, can be written in compact form as:

$$(al+b)\frac{dl}{dt} - cl = d \tag{29}$$

Eq. (29), therefore, describes the advancement of the interface inside the capillary tube for the case in which l lies between $L-l_g$ and L.

4. Verification, and validation

In this section, we provide comparisons with CFD analysis of two cases representing a wetting and nonwetting ganglions, ignoring the gravity. For this system, $a_g = 0$, and during the first flow pattern in which the ganglion is totally encompassed inside the tube, the location of the meniscus is determined by $l(t) = (\Delta p/a_\mu)t$. This formula is used initially assuming that $\Delta p_c = 0$. This flow patterns ends when $l = L - l_g$ after a time period of $t_I = a_\mu(L-l_g)/\Delta p$. When the ganglion starts to break through the exit, the second flow pattern starts and, in this case, we have Eq. (29) modifies to:

$$(al+b)\frac{dl}{dt} = d \tag{30}$$

Integration yields:

$$\frac{a}{2}l^2 + bl = dt + C \tag{31}$$

where C is the constant of integration, which may be calculated knowing the initial condition. Therefore, when $t = t_I$, and $l = L - l_g$, the constant of integration, C, is:

$$C = \frac{a}{2}(L-l_g)^2 + b(L-l_g) - dt_I \tag{32}$$

Substitution into Eq. (31), one obtains:

$$t = \frac{a}{2d}l^2 + \frac{b}{d}l - \left[\frac{a}{2d}(L-l_g)^2 + \frac{b}{d}(L-l_g) - t_I\right] \tag{33}$$

Collecting terms and simplification yields the following algebraic equation:

$$t = \frac{aL^2}{2d}\left[\frac{l^2}{L^2} - \frac{(L-l_g)^2}{L^2}\right] + \frac{bL}{d}\left[\frac{l}{L} - \frac{(L-l_g)}{L}\right] + t_I \tag{34}$$

In the considered setup, when gravity is neglected, the parameter d equals $\Delta p/|p_c| \pm p_c/|p_c|$. It is to be mentioned that, apart from the speculation of slowly moving meniscus, the dynamic contact angle should be used for the two flow regimes of the ganglion. Even though there exist models that correlate the dynamic contact angle with the velocity (or more specifically the capillary number), these models may be valid for some special cases (Salama, 2021a). In this work, the problem is even more complicated by the fact that there exist two contact angles associated with the two interfaces of the ganglion inside the capillary tube. It is beyond the scope of this work to review the different models for estimating the dynamic contact angle. Interested readers, however, may refer to the ample works of several authors who have considered this topic (Payatakes, 1982; Wu et al., 2017; Siebold et al., 2020). In this work, however, the dynamic contact angles have been used as a fitting parameter that is tuned to match the CFD results. The fitting process involves generating the normalized volume curves assuming static contact angle conditions. Then the receding contact angle is adjusted to fit the general behavior of the normalized volume profile for the second flow regime (i.e., after the ganglion has broken through the exit). The advancing contact angle is then tuned to match the location of the receding meniscus at the end of the first flow regime. In

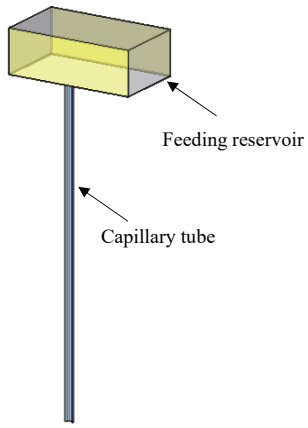

Fig. 4. Schematic of the computational domain. The parallelopiped at the top is a reservoir of the invading fluid and the capillary tube attached to the reservoir is where the ganglion exists.

the next section, a description of the computational setup that is used to provide comparison exercises for validation purposes is introduced.

4.1 Computational setup and CFD results

The computational setup built for the purpose of providing a framework for validation represents a rectangular parallelepiped region that defines a reservoir and a capillary pipe attached to the reservoir. The reservoir has dimensions of $5 \times 4 \times 3$ μm and the capillary tube has a diameter of 0.4 μm and a length of 15 μm (i.e., L/D ratio of approximately 40), as shown schematically in Fig. 4. This setup has been used in ample previous works (Zoubeik et al., 2018; Salama, 2020a, 2020b, 2020c, 2020d, 2021b, 2021c; Echakouri et al., 2021) for which sensitivity analysis of the adequacy of mesh resolution as well as the appropriate discretization schemes for the different terms contributing to the governing equations have been explored and will not, therefore, be repeated here. Furthermore, the governing equations in the context of volume of fluid modeling have also been described in previous other works (Zoubeik et al., 2018; Echakouri et al., 2021; Salama, 2021b, 2021c).

Two cases have been explored in this work representing; namely, 1) a nonwetting ganglion displaced by a wetting phase and 2) a wetting ganglion displaced by a nonwetting phase. In both scenarios, a number of cases of different viscosity contrasts of the two phases have been considered. In all the studied scenarios, a ganglion is initiated at the inlet of the capillary tube of a length of one third the length of the tube (i.e., l_g = 5 μm). For the nonwetting ganglion scenario, the ganglion is considered having a static contact angle of 135° and is 45° for the wetting ganglion scenario. In both cases, the surface tension has been considered as 0.025 N/m and the

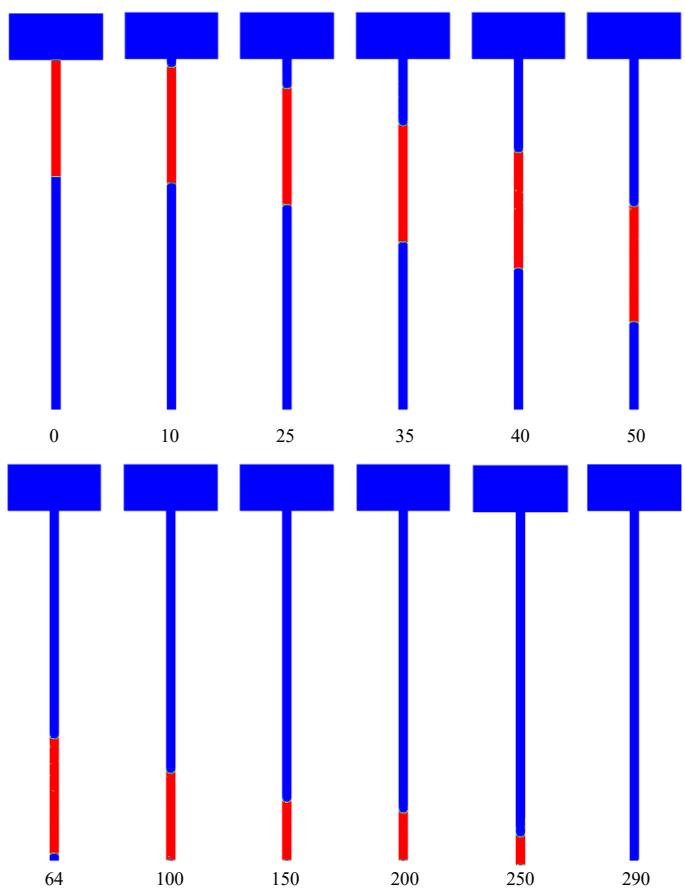

Fig. 5. Snapshots of the location of a wetting ganglion inside a capillary tube. The followings are the operating conditions and properties of both fluids: Δp = 2.5 bars, γ = 0.025 N/m, θ = 45°, μ_w = 0.01 Pa·s, μ_{nw} = 0.001 Pa·s, λ = 0.1.

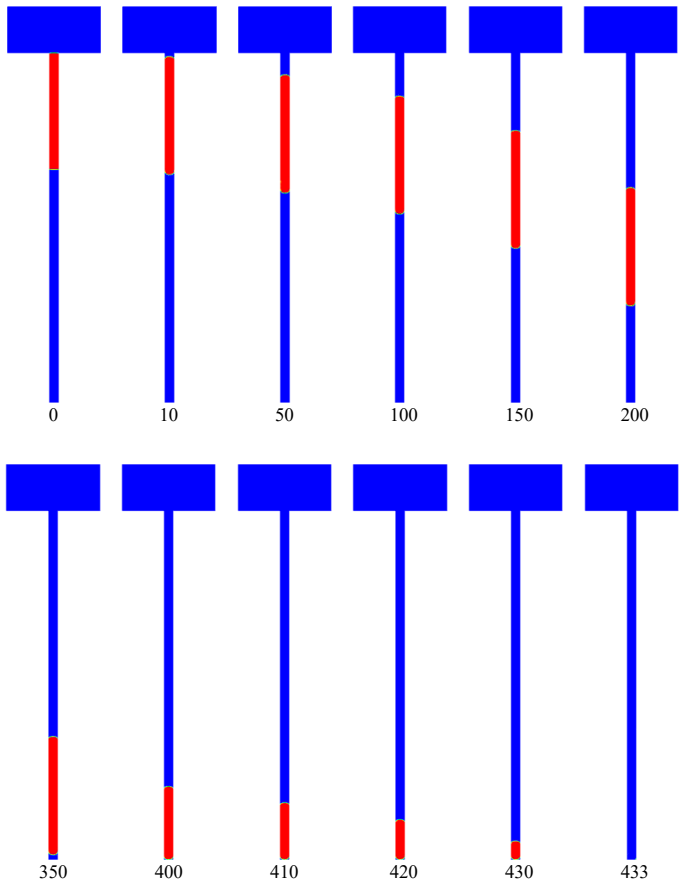

Fig. 6. Snapshots of the location of a nonwetting ganglion inside a capillary tube. The followings are the operating conditions and properties of both fluids: Δp = 2.5 bars, γ = 0.025 N/m, θ = 135°, μ_w = 0.001 Pa·s, μ_{nw} = 0.01 Pa·s, λ = 0.1.

pressure difference along the capillary tube of 2.5 bars.

Fig. 5 shows snapshots of the ganglion inside the capillary tube at different times for the case in which the ganglion is wetting. In this case, the two interfaces of the ganglion assume concave shapes. Two cases with respect to the viscosity contrast have been considered; namely, 1) when λ = 0.1 (i.e., the invading fluid is less viscous than the ganglion), and 2) when λ = 10 (i.e., the invading fluid is more viscous than the ganglion). As depicted in Fig. 5, for the case when λ = 10, the ganglion advances inside the tube at a constant rate until the advancing interface reaches the exit, then the rate decreases during the increase in the volume of the invading fluid which is more viscous. On the other hand, when the ganglion is nonwetting, the two interfaces assume convex shape. Again, during the displacement of the ganglion, when it is fully contained within the tube, the ganglion is displaced at a constant rate. Once the leading interface has reached the exit of the tube, the displacement of the receding interface accelerates or decelerates dependent on the viscosity ratio. Therefore, if the viscosity ratio is larger than one, the receding interface decelerates, and accelerates otherwise. This is depicted in Fig. 6 which shows the case of a nonwetting ganglion with λ = 0.1 for which case it takes less time for the receding interface to clear the tube.

4.2 Validation exercises

Now it is important to establish confidence in the introduced model by providing comparisons with the conducted CFD analysis. The comparisons are done by comparing the normalized volume of both the invading fluid and the ganglion (both are normalized by the volume of the tube) with those calculated by the developed model. It is clear that the volume of both the invading fluid and the ganglion remains constant during the period when the ganglion is fully contained inside the tube. Once the leading interface of the ganglion has reached the exit of the tube, the volume of the invading fluid increases until eventually it fills the tube and the volume of the ganglion decreases until the ganglion totally exits the tube. The viscosity contrast controls the rate at which the ganglion leaves the tube. That is, when the viscosity contrast is larger than one (i.e., $\lambda > 1$) the ganglion leaves at a slower rate as the resistance increases by the increase in the volume of the more viscous fluid and vice versa. In all the examples considered in these validation exercises, gravity has been ignored.

Fig. 7 shows the case of a wetting ganglion inside a capillary tube whose static contact angle is set to θ = 45° and is displaced by a nonwetting fluid with two viscosity contrasts; namely, λ = 0.1, and λ = 10. For the case when λ = 0.1 (i.e., the ganglion is 10 times more viscous than the invading fluid), the overall resistance of the two-phase system inside the tube

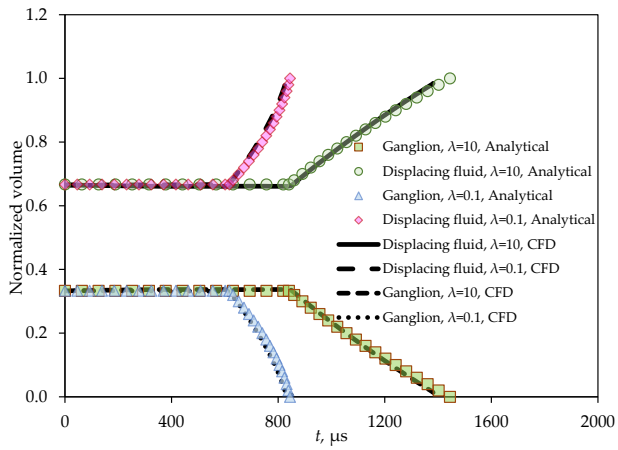

Fig. 7. Comparisons between the normalized volumes of both the invading fluid and the ganglion calculated using both CFD and the developed analytical model for the case of wetting ganglion under two viscosity contrasts; namely λ = 0.1 and λ = 10.

is less than that when λ = 10 (i.e., the invading fluid is 10 times more viscous). The difference is manifested in the time it takes for the invading fluid to fill in the tube. As depicted, it took longer for the ganglion to reach the exit of the tube when λ = 10, than it is when λ = 0.1. That is when λ = 10, two third of the tube is filled with the more viscous fluid than when λ = 0.1. Furthermore, the wetting ganglion clears the tube at a faster rate when λ = 0.1, than it is when λ = 10. This is, again, because in the first case the less viscous fluid replaces the more viscous one, and therefore, the overall resistance decreases. The comparisons show very good match as depicted in Fig. 7. It is to be noted that, in both scenarios of a wetting ganglion, the interfacial tension force of the receding interface when the leading interface has left the tube opposes the direction of the flow as depicted in Fig. 3(a).

On the other hand, for the cases where the ganglion is nonwetting, several scenarios of viscosity different contrasts were considered; namely, λ = 0.2, 0.1, 0.02, and 0.01. In these scenarios, the larger the viscosity of the invading fluid (i.e., the smaller the viscosity ratio) the longer it takes for the ganglion to clear off the tube. This is manifested in Fig. 8, which shows the profiles of normalized volume of the invading fluid (Fig. 8(a)) and of the ganglion (Fig. 8(b)). As seen, the normalized volume of both the invading fluid and the ganglion remains constant during the period where the ganglion is contained within the tube. When the ganglion breaks through the exit, the invading fluid advances at a faster pace because its viscosity is less than the viscosity of the ganglion. It is also worth mentioning that the interfacial tension force of the receding interface for this scenario is in the direction of the flow as depicted in Fig. 3(b).

5. Discussions and Analysis

In this section, parametric analysis of the influence of the viscosity ratio, contact angle and affinity state of the ganglion is presented. The study considers the idealized cases when the contact angle assumes the static condition. In this case, both the advancing and the receding interfaces assume the same contact angle and will not, therefore, contribute any net force when the ganglion is totally contained inside the tube.

We start with the case in which the invading fluid is more viscous than the ganglion (i.e., λ>1). For this system, when the ganglion is fully contained inside the tube it advances uniformly and the menisci advance linearly in time. The first case considers a neutral ganglion for which the interface assumes a contact angle of 90°. As shown in Fig. 9(a), the ganglion advances first linearly, then nonlinearly once the advancing interface has break through the exit of the tube. Furthermore, the lager the viscosity ratio, the larger the elapsed time till the ganglion has left the tube. It is to be noted that, in this scenario, interfacial tension forces do not play any role. Similarly, Fig. 9(b) depicts the case of a nonwetting, less viscous ganglion with the static contact angle of 45°. In this case, the ganglion, once starts to break through the exit, would experience an additional force in the direction of the flow due to capillarity. This force would result in clearing the

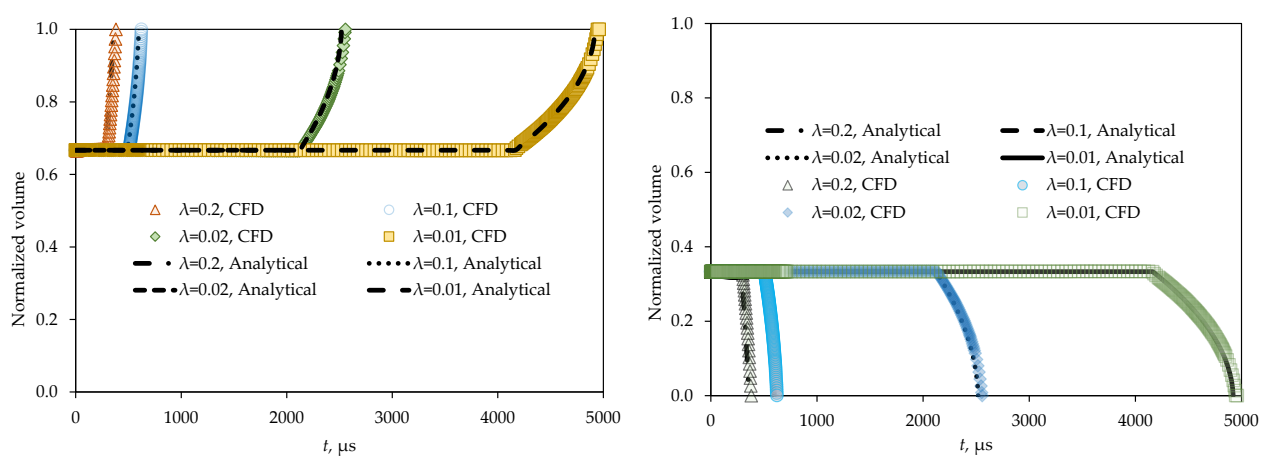

(a) Normalized volume of the displacing fluid

(b) Normalized volume of the ganglion

Fig. 8. Variations of the normalized volumes of both the invading fluid and of the ganglion with time as determined via the considered CFD simulation and the analytical model.

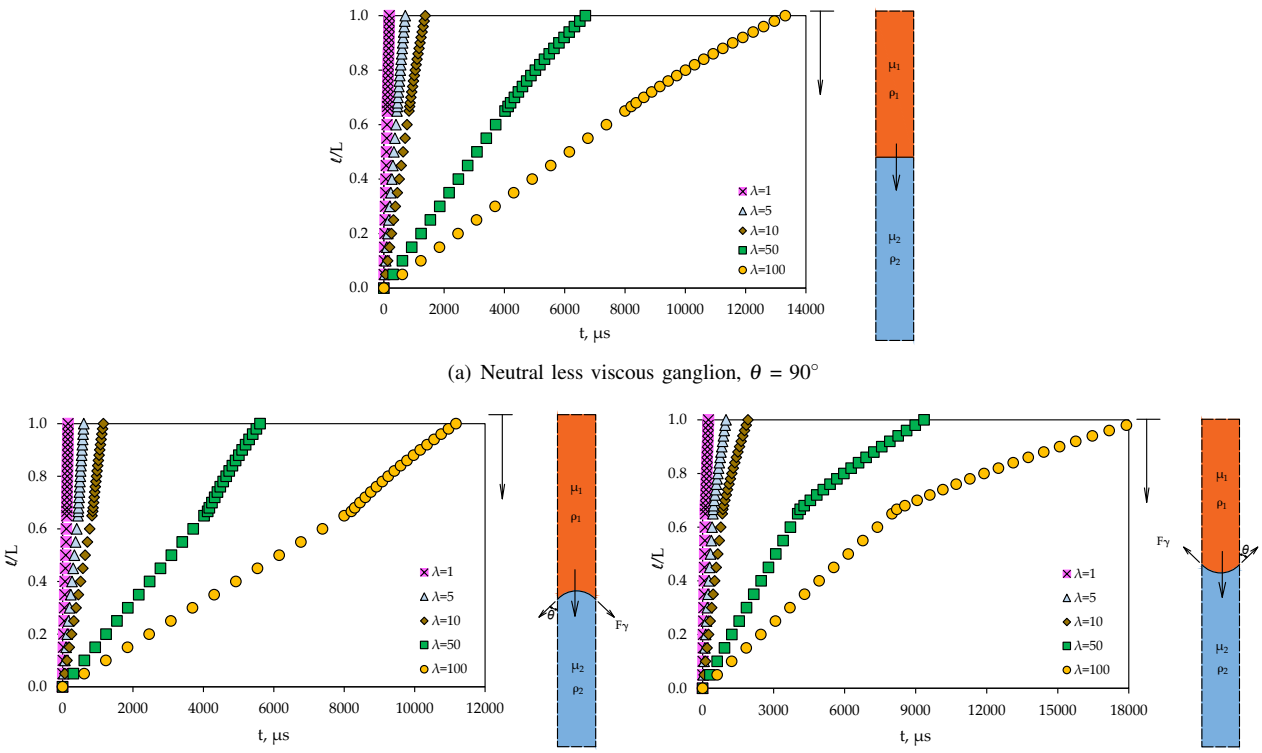

(a) Neutral less viscous ganglion, θ = 90°

(b) Nonwetting less viscous ganglion, θ = 45°

(c) Wetting less viscous ganglion, θ = 60°

Fig. 9. Profiles of the normalized distance of the receding miscues (normalized by the length of the tube) for the cases when the displacing fluid is more viscous than the ganglion for both wetting and nonwetting ganglions.

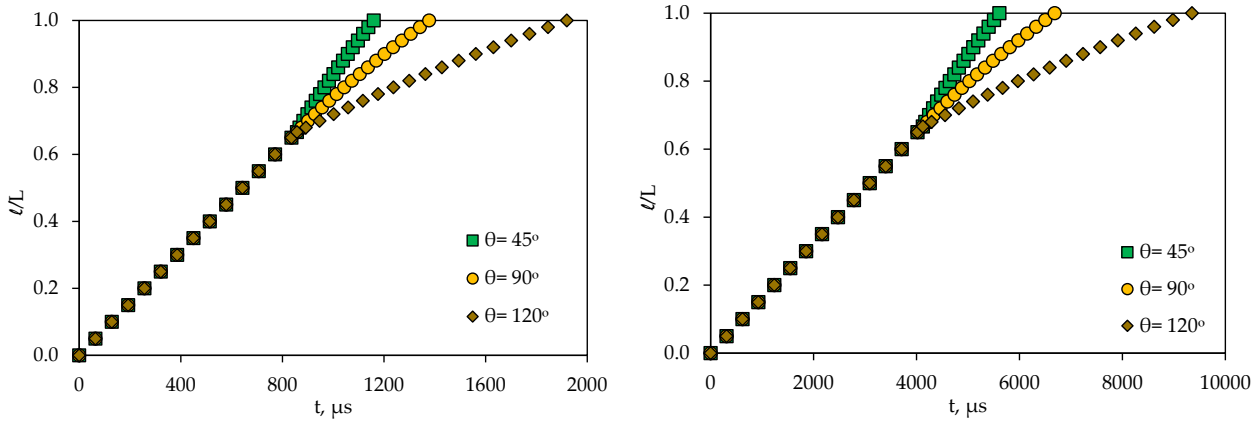

(a) λ = 10

(b) λ = 50

Fig. 10. Comparisons of the profiles of the advancement of the ganglion in the tube for the following viscosity ratios: (a) λ = 10, and (b) λ = 50 for different static contact angles.

ganglion from the tube faster. This is manifested in the change in the slope of the normalized location of the meniscus when the leading interface has break through the tube. This is also manifested in the elapsed time when the ganglion has cleared the tube, which is less than that of the previous case. When the less viscous ganglion is wetting with a contact angle of 60°, as shown in Fig. 9(c), interfacial tension forces reverse its role. That is once the leading interface of the ganglion has break through the exit of the tube, interfacial tension force becomes opposite to the direction of motion of the flow. This results again in changing the slope of the curve and also increases the elapsed time till the ganglion clear off the tube.

It is interesting to compare between the effects of the contact angle for the same viscosity ratio on the normalized location of the meniscus. This is depicted in Figs. 10(a) and 10(b) which shows two cases, namely, a) when λ = 10, and b) when λ = 50. One scenario considers a nonwetting ganglion (corresponding to a contact angle of 45°) and another scenario for a wetting ganglion for which the contact angle is 120°. In Fig. 10(a), it is clear that it is faster to clear off the ganglion

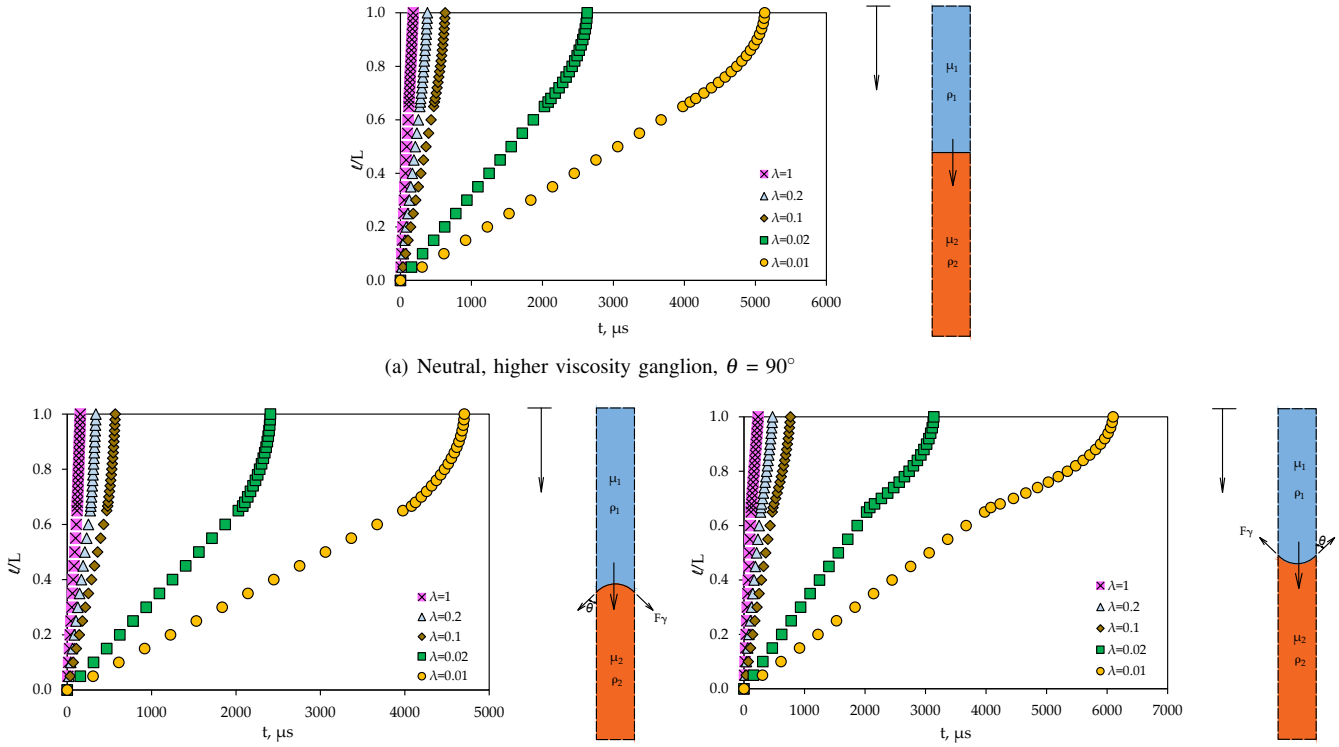

(a) Neutral, higher viscosity ganglion, θ = 90°

(c) Nonwetting, higher viscosity ganglion, θ = 45°

(e) Wetting, higher viscosity ganglion, θ = 60°

Fig. 11. Profiles of the normalized distance of the receding miscues (normalized by the length of the tube) for the cases when the displacing fluid is more viscous than the ganglion for both wetting and nonwetting ganglions.

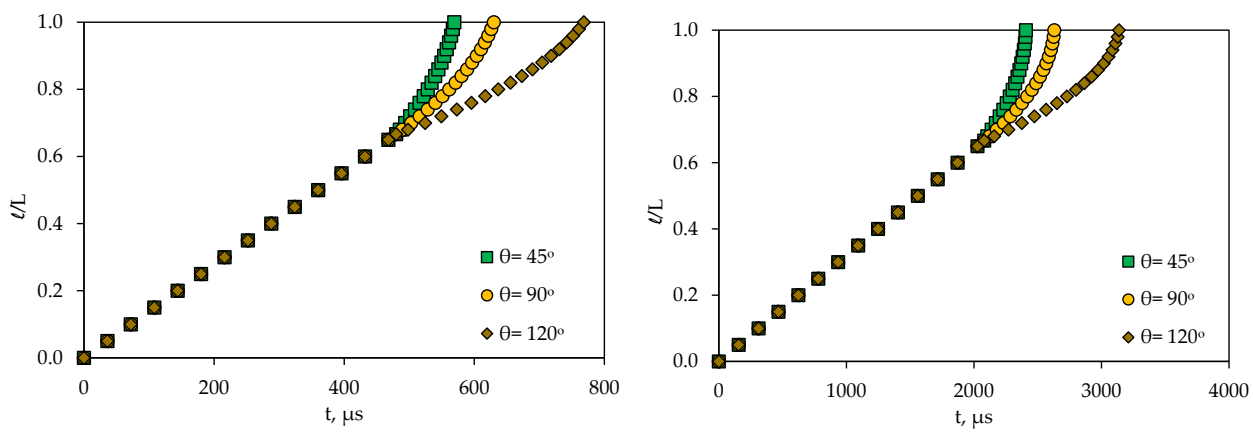

(a) λ = 0.1

(b) λ = 0.02

Fig. 12. Comparisons of the profiles of the advancement of the ganglion in the tube for the following viscosity ratios: (a) λ = 0.1, and (b) λ = 0.02 for different static contact angles.

when the ganglion is nonwetting than it is when the ganglion is wetting. Again, this is a consequence of the interfacial tension force of the receding interface, which is in the direction of the flow when the ganglion is nonwetting and opposite to the direction of the flow when the ganglion is wetting. Similar behavior is also noticed for the case when λ = 50, as shown in Fig. 10(b) albeit longer elapsed time.

In the previously studied cases the invading fluid has been considered more viscous than the ganglion. In the next example, the opposite scenario in which the invading fluid is considered less viscous than the ganglion (i.e., λ<1) is studied. In this case, the overall resistance of the fluids to the flow is less than the previously studied cases. This is a consequence of the fact that the less viscous fluid occupies twice as much the volume of the ganglion. Fig. 11 shows three cases; namely, a) a neutral ganglion, b) a nonwetting ganglion, and c) a wetting ganglion. In the first case, interfacial tension does not play any role in the two flow regimes. During the first flow regime (i.e., when the ganglion is fully contained inside the tube), linear variation of the normalized volume of

the two phases is observed. Again, this is a manifestation of the constancy of the driving and resistive forces. Once the leading interface of the ganglion has left the tube, the friction force continues to decrease resulting in the receding meniscus to accelerate, Fig. 11(a).

When the ganglion is nonwetting, the same linear variation of the normalized volumes is observed during the first flow regime. During the second flow regime, however, the net interfacial tension force of the receding interface is in the direction of the flow and this results in extra acceleration due to this additional force, Fig. 11(b).

The last case depicts the scenario in which the ganglion is wetting. In this case, during the second flow regime, the surface tension force is in the direction opposite to the flow direction and this results in the ganglion to take more time until it clears off the tube, Fig. 11(c).

To compare between the effects of the contact angle for the same viscosity ratio, Fig. 12 shows comparisons between the different contact angle scenarios for two cases of viscosity contrasts; namely $\lambda = 0.1$, and $\lambda = 0.02$. From these figures (Figs. 11(a) and 11(b)) it is clear that it takes longer for the ganglion to clear off the tube when it is wetting.

6. Conclusions

In this work, the scenarios of displacing a wetting/non-wetting ganglion by another immiscible fluid in capillaries have been studied. A model is developed that divide the flow regime into two. The first flow regime depicts the time in which the ganglion is contained inside the capillary tube and the second depicts the flow regime in which the ganglion starts to break through the exit of the tube. In the first regime, four forces appear; namely, pressure force, gravity, capillarity, and viscous resistance force. In this regime, these forces are constant and therefore, the ganglion advances uniformly inside the tube. Once the ganglion starts to exit the tube, this marks the second flow regime. In this case, the friction force increases when the displacing fluid is more viscous than the ganglion, and decreases otherwise. Furthermore, the interfacial tension force will be in the direction of the flow when the ganglion in nonwetting, and opposite to the flow if otherwise. The model also considers the case of a quasistatic movement of the ganglion in the tube. In this case, the contact angles of the receding and the advancing interfaces of the ganglion may be considered the same and interfacial tension force may be ignored in the first flow regime. A CFD study has also been conducted to provide framework for verification and validation of the developed model. Comparisons show very good match between the model and the CFD study, which builds confidence in the modeling approach.

Conflict of interest

The authors declare no competing interest.

Open Access This article is distributed under the terms and conditions of the Creative Commons Attribution (CC BY-NC-ND) license, which permits unrestricted use, distribution, and reproduction in any medium, provided the original work is properly cited.

References

Abdus S., Iqbal, G. M., Buchwalter, J. L. Practical Enhanced Reservoir Engineering: Assisted With Simulation Software. Oklahoma, USA, Pennwell, 2008.

Ahmed, T. Principles of Waterflooding, in Reservoir Engineering Handbook, edited by T. Ahmed, Gulf Professional Publishing, USA, pp. 901-1107, 2019.

Alemu, B. L., Aker, E., Soldal, M., et al. Influence of CO_2 on rock physics properties in typical reservoir rock: A CO_2 flooding experiment of brine saturated sandstone in a CT-scanner. Energy Procedia, 2011, 4: 4379-4386.

Almetwally, A. G., Jabbari, H. Finite-difference simulation of coreflooding based on a reconstructed CT scan; modeling transient oscillating and pulse decay permeability experiment. Journal of Petroleum Science and Engineering, 2020, 192: 107260.

Arab, D., Kantzas, A., Bryant, S. L. Water flooding of oil reservoirs: Effect of oil viscosity and injection velocity on the interplay between capillary and viscous forces. Journal of Petroleum Science and Engineering, 2020, 186: 106691.

Bageri, B. S., Adebayo, A. R., Al Jaberi, J., et al. Evaluating drilling fluid infiltration in porous media-comparing NMR, gravimetric, and X-ray CT scan methods. Journal of Petroleum Science and Engineering, 2021, 198: 108242.

Bao, K., Salama, A., Sun, S. Numerical investigation on the effects of a precursor wetting film on the displacement of two immiscible phases along a channel. Flow, Turbulence and Combustion, 2016, 96(3): 757-771.

Bao, K., Salama, A., Sun, S. Flow split characterization of two immiscible phases with different wettability scenarios: A numerical investigation using a coupled Cahn-Hilliard and Navier-Stokes system. International Journal of Multiphase Flow, 2018, 100: 172-185.

Batchelor, G. K. An Introduction to Fluid Dynamics. Cambridge, United Kingdom, Cambridge University Press, 2000.

Benilova, E. S. The dynamics of liquid films, as described by the diffuse-interface model. Physics of Fluids, 2020, 32(11): 112103.

Bijeljic, B., Markicevic, B., Navaz, H. K. Capillary climb dynamics in the limits of prevailing capillary and gravity force. Physical Review E, 2011, 83(5): 056310.

Blunt, M. J. Flow in porous media-pore-network models and multiphase flow. Current Opinion in Colloid and Interface Science, 2001, 6(3): 197-207.

Blunt, M. J., Jackson, M. D., Piri, M., et al. Detailed physics, predictive capabilities and macroscopic consequences for pore-network models of multiphase flow. Advances in Water Resources, 2002, 25(8-12): 1069-1089.

Cai, J., Hu, X., Standnes, D. C., et al. An analytical model for spontaneous imbibition in fractal porous media including gravity. Colloids and Surfaces A: Physicochemical and Engineering Aspects, 2012, 414: 228-233.

Cai, J., Jin, T., Kou, J., et al. Lucas-washburn equation-based modeling of capillary-driven flow in porous systems.

Langmuir, 2021, 37(5): 1623-1636.

Cai, J., Yu, B., Zou, M., et al. Fractal analysis of invasion depth of extraneous fluids in porous media. Chemical Engineering Science, 2010, 65(18): 5178-5186.

Cnudde, V., Boone, M., Dewanckele, J., et al. 3D characterization of sandstone by means of X-ray computed tomography. Geosphere, 2011, 7(1): 54-61.

De Mello, E. V. L., da Silveira Filho, O. T. Numerical study of the Cahn-Hilliard equation in one, two and three dimensions. Physica A: Statistical Mechanics and its Applications, 2005, 347: 429-443.

Dullien, F. A. L., El-Sayed, M. S., Batra, V. K. Rate of capillary rise in porous media with nonuniform pores. Journal of Colloid and Interface Science, 1977, 60(3): 497-506.

Echakouri, M., Salama, A., Henni, A. Experimental and computational fluid dynamics investigation of the deterioration of the rejection capacity of the membranes used in the filtration of oily water systems. ACS ES&T Water, 2021, 1(3): 728-744.

Grunau, D., Chen, S., Eggert, K. A lattice Boltzmann model for multiphase fluid flows. Physics of Fluids A: Fluid Dynamics, 1993, 5(10): 2557-2562.

Guo, Z. Well-balanced lattice Boltzmann model for two-phase systems featured. Physics of Fluids, 2021, 33(3): 031709.

Hammecker, C., Mertz, J. D., Fischer, C., et al. A geometrical model for numerical simulation of capillary imbibition in sedimentary rocks. Transport in Porous Media, 1993, 12(2): 125-141.

Huang, X., Zhou, W., Deng, D. Validation of pore network modeling for determination of two-phase transport in fibrous porous media. Scientific Reports, 2020, 10(1): 20852.

Jha, K. N. Residual Oil in Reservoirs Problems and Prospects, in Energy Developments: New Forms, Renewables, Conservation, Pergamon, edited by F. A. Curtis, Pergamon Press, Canada, pp. 41-48, 1984.

Joekar-Niasar, V., Hassanizadeh, S. M. Effect of fluids properties on non-equilibrium capillarity effects: Dynamic pore-network modeling. International Journal of Multiphase Flow, 2011, 37(2): 198-214.

Joekar-Niasar, V., Hassanizadeh, S. M. Analysis of fundamentals of two-phase flow in porous media using dynamic pore-network models: A review. Critical Reviews in Environmental Science and Technology, 2012, 42(18): 1895-1976.

Lamura, A., Gonnella, G., Yeomans, J. M. A lattice Boltzmann model of ternary fluid mixtures. Europhysics Letters, 1999, 45(3): 314-320.

Lucas, R. Rate of capillary ascension of liquids. Kollid Z, 1918, 23(15): 15-22.

Madonna, C., Almqvist, B. S. G., Saenger, E. H. Digital rock physics: Numerical prediction of pressure-dependent ultrasonic velocities using micro-CT imaging. Geophysical Journal International, 2012, 189(3): 1475-1482.

Mogensen, K., Masalmeh, S. A review of EOR techniques for carbonate reservoirs in challenging geological settings. Journal of Petroleum Science and Engineering, 2020, 195: 107889.

Montazeri, H., Zandavi, S. H., Bazylak, A. Sharp interface models for two-phase flows: Insights towards new approaches. Computer Methods in Applied Mechanics and Engineering, 2017, 322: 238-261.

Nordhaug, H. F., Celia, M., Dahle, H. K. A pore network model for calculation of interfacial velocities. Advances in Water Resources, 2003, 26(10): 1061-1074.

Pan, L., Lou, J., Li, H., et al. A diffuse interface model for two-phase flows with phase transition. Physics of Fluids, 2019, 31(9): 092112.

Payatakes, A. C. Dynamics of oil ganglia during immiscible displacement in water-wet porous media. Annual Review of Fluid Mechanics, 1982, 14(1): 365-393.

Qin, C. Z., van Brummelen, H. A dynamic pore-network model for spontaneous imbibition in porous media. Advances in Water Resources, 2019, 133: 103420.

Ramanathan, R., Shehata, A. M., Nasr-El-Din, H. A. Effect of rock aging on oil recovery during water-alternating-CO_2 injection process: An interfacial tension, contact angle, coreflood, and CT scan study. Paper SPE 179674 Presented at the SPE Improved Oil Recovery Conference, Tulsa, Oklahoma, USA, 11-13 April, 2016.

Raoof, A., Hassanizadeh, S. M. A new method for generating pore-network models of porous media. Transport in Porous Media, 2010, 81(3): 391-407.

Raoof, A., Nick, H. M., Hassanizadeh, S. M., et al. Poreflow: A complex pore-network model for simulation of reactive transport in variably saturated porous media. Computers and Geosciences, 2013, 61: 160-174.

Regaieg, M., Moncorgé, A. Adaptive dynamic/quasi-static pore network model for efficient multiphase flow simulation. Computional Geosciences, 2017, 21(4): 795-806.

Salama, A. Investigation of the onset of the breakup of a permeating oil droplet at a membrane surface in crossflow filtration: A new model and CFD verification. International Journal of Multiphase Flow, 2020a, 126: 103255.

Salama, A. On the breakup of a permeating oil droplet in crossflow filtration: Effects of viscosity contrast. Physics of Fluids, 2020b, 32(7): 072101.

Salama, A. On the estimation of the leaked volume of an oil droplet undergoing breakup in crossflow filtration: CFD investigation, scaling, and a macroscopic model. Separation and Purification Technology, 2020c, 252: 117459.

Salama, A. Simplified formula for the critical entry pressure and a comprehensive insight into the critical velocity of dislodgment of a droplet in crossflow filtration. Langmuir, 2020d, 36(32): 9634-9642.

Salama, A. A generalized analytical model for estimating the rate of imbibition/drainage of wetting/nonwetting fluids in capillaries. Chemical Engineering Science, 2021a, 243: 116788.

Salama, A. Coalescence of an oil droplet with a permeating one over a membrane surface: Conditions of permeation, recoil, and pinning. Langmuir, 2021b, 37(12): 3672-3684.

Salama, A. Critical entry pressure of a droplet pinning over multitude of pore openings. Physics of Fluids, 2021c, 33(3): 032114.

Salama, A., Amin, M. F. E., Kumar, K., et al. Flow and transport in tight and shale formations: A review. Geofluids, 2017, 2017: 4251209.

Sato, Y., Ničeno, B. A sharp-interface phase change model for a mass-conservative interface tracking method. Journal of Computational Physics, 2013, 249: 127-161.

Sheng, J. J. Alkaline-polymer Flooding, in Enhanced Oil Recovery Field Case Studies, edited by J. J. Sheng, Gulf Professional Publishing, USA, pp. 169-178, 2013.

Siebold, A., Nardin, M., Schultz, J., et al. Effect of dynamic contact angle on capillary rise phenomena. Colloids and Surfaces A: Physicochemical and Engineering Aspects, 2020, 161(1): 81-87.

Speight, J. G. Upgrading by Hydrocracking, in Heavy Oil Recovery and Upgrading, edited by J. G. Speight, Gulf Professional Publishing, USA, pp. 467-528, 2019.

Tummons, E. N., Tarabara, V. V., Chew, J., et al. Behavior of oil droplets at the membrane surface during crossflow microfiltration of oil-water emulsions. Journal of Membrane Science, 2016, 500: 211-224.

Washburn, E. W. The dynamics of capillary flow. Physical Review, 1921, 17(3): 273-283.

Won, J., Lee, J., Burns, S. E. Upscaling polydispersed particle transport in porous media using pore network model. Acta Geotechnica, 2021, 16(2): 421-432.

Wu, P., Nikolov, A. D., Wasan, D. T. Capillary rise: Validity of the dynamic contact angle models. Langmuir, 2017, 33(32): 7862-7872.

Xiong, Q., Baychev, T. G., Jivkov, A. P. Review of pore network modelling of porous media: Experimental characterisations, network constructions and applications to reactive transport. Journal of Contaminant Hydrology, 2016, 192: 101-117.

Xu, X., Di, Y., Yu, H. Sharp-interface limits of a phase-field model with a generalized Navier slip boundary condition for moving contact lines. Journal of Fluid Mechanics, 2018, 849: 805-833.

Zhang, T., Salama, A., Sun, S., et al. Pore network modeling of drainage process in patterned porous media: A quasi-static study. Journal of Computational Science, 2015, 9: 64-69.

Zhong, H., Wang, X., Salama, A., et al. Quasistatic analysis on configuration of two-phase flow in Y-shaped tubes. Computers and Mathematics with Applications, 2014, 68(12): 1905-1914.

Zoubeik, M., Salama, A., Henni, A. A novel antifouling technique for the crossflow filtration using porous membranes: Experimental and CFD investigations of the periodic feed pressure technique. Water Research, 2018, 146: 159-176.